separations

MDPI

Article

Photocatalytic Removal of Crystal Violet Dye Utilizing Greenly Synthesized Iron Oxide Nanoparticles

Mohamed Taha Yassin *, Fatimah O. Al-Otibi and Abdulaziz A. Al-Askar

Department of Botany and Microbiology, College of Science, King Saud University, P.O. Box 2455, Riyadh 11451, Saudi Arabia; falotibi@ksu.edu.sa (F.O.A.-O.); aalaskara@ksu.edu.sa (A.A.A.-A.)
* Correspondence: myassin2.c@ksu.edu.sa

Abstract: The presence of synthetic industrial dyes in the environment poses significant risks to aquatic ecosystems, human health, and economies. This study aims to synthesize iron oxide nanoparticles (IONPs) using a green method, analyze them using physicochemical techniques, and examine the effectiveness with which they photocatalytically degrade crystal violet dye in sunlight. Fourier transform infrared spectroscopy (FTIR) analysis revealed that the biogenic IONPs showed a UV peak at a wavelength of 241 nm, with functional groups including phenols, alkynes, and alkenes. X-ray diffraction (XRD) analysis confirmed the amorphous nature of the bioinspired IONPs. The mean diameter of the biogenic IONPs was 49.63 ± 9.23 nm, and they had a surface charge of −5.69 mV. The efficiency with which the synthesized IONPs removed the crystal violet dye was evaluated under dark and sunlight conditions. The removal efficiency was found to be concentration and time dependent, with a peak removal percentage of 99.23% being achieved when the IONPs were exposed to sunlight for 210 min. The biogenic IONPs also demonstrated antioxidant activity, with a relative IC_{50} value of 64.31 µg/mL. In conclusion, biogenic IONPs offer a viable and environmentally friendly approach for eradicating industrial synthetic dyes and remediating contaminated environments and aquatic ecosystems.

Keywords: green synthesis; *Camellia sinensis*; characterization; dye removal; antioxidant

Citation: Yassin, M.T.; Al-Otibi, F.O.; Al-Askar, A.A. Photocatalytic Removal of Crystal Violet Dye Utilizing Greenly Synthesized Iron Oxide Nanoparticles. *Separations* **2023**, *10*, 513. https://doi.org/10.3390/separations10090513

Academic Editor: Anastasia D. Pournara

Received: 28 August 2023
Revised: 11 September 2023
Accepted: 15 September 2023
Published: 17 September 2023

1. Introduction

The presence of water is crucial for both biological and industrial processes as it plays a vital role in sustaining life and facilitating various industrial activities [1]. However, the limited availability of water in several regions has led to significant adverse consequences in terms of health and economic burdens [2]. The non-utilization of water contaminated with substances such as organic dyes is a contributing factor to water shortages [3]. The primary source of wastewater pollution is believed to be the discharge of organic dyes originating from several industrial sectors, such as the paper, textile, paint, plastic, and rubber industries [4]. Approximately 15–20% of organic dyes are discharged into wastewater during various synthesis or processing activities in the aforementioned sectors [5]. The existence of these substances in wastewater has significant implications for both human health and the environment [6]. Certain dyes have been reported to be mutagenic and hazardous substances and thus pose a potential danger to human health [7]. Moreover, trace dyes have a high level of resistance to biodegradation by indigenous flora, and this may potentially lead to the occurrence of allergic dermatitis or skin irritations [8]. A range of chemical, physical, and biological processes have been investigated for the purpose of eliminating organic dyes from wastewater [9]. These processes include precipitation, chemical oxidation, coagulation, filtration, solvent extraction, electrochemical and membrane processes, ultrasonic techniques, adsorption, reverse osmosis, and other biological processes [10]. The adsorption technique was determined to be more effective than other wastewater treatment technologies due to its cost-effectiveness, versatility, simplicity, ease of implementation,

and resistance to detrimental pollutants [11]. Various materials, such as zeolites, industrial byproducts, activated carbons, clays, agricultural wastes, biomass, and polymeric materials, have been employed for the synthesis of dye adsorbents [12]. Nevertheless, these adsorbents possess restricted adsorption capacities and separation efficiencies, and these impose limitations on their practical use [13]. Nanoparticles possess several advantageous characteristics, including a substantial specific surface area, low diffusion resistance, enhanced adsorption capacity, and an ability to quickly attain adsorption equilibrium [14]. The use of magnetic nanoparticles facilitates convenient separation by the application of an external magnetic field [15]. Nanotechnology has evolved as a dynamic and innovative scientific field that seeks to develop nanosystems for addressing many challenges in the realms of health and the environment [16]. Nanocrystalline materials are widely utilized in several disciplines owing to their physiochemical characteristics, which are primarily attributed to their higher surface area-to-volume ratio [17]. Iron oxide nanoparticles are widely recognized as exceptional materials for many environmental and therapeutic purposes due to their desirable attributes, such as their minimal band gaps, chemical uniformity, magnetic capabilities, and other distinctive traits [18]. Various methods have been employed for the synthesis of iron oxide nanoparticles, including co-precipitation, the polyol technique, electrochemical synthesis, the sol-gel method, microwave irradiation, chemical vapor deposition, and the pulsed laser method [19]. However, these techniques have certain limitations as they often involve the use of highly toxic reducing agents such as borohydride and sodium hydrazine [20]. Recently, researchers have developed environmentally sustainable ways of producing of nanoparticles, such as biosynthesis (also known as green synthesis). In recent years, comprehensive investigations have been conducted to explore the biological production of nanoparticles using a diverse range of microorganisms, including bacteria, fungi, actinomycetes, algae, and yeasts [21]. Nevertheless, the utilization of microorganisms has certain drawbacks, such as (i) the sluggish rates of synthesis; (ii) the requirement for several steps, including culture preparation and isolation; (iii) the factor of time consumption; and (iv) the restricted ranges of sizes and forms [22]. In order to address these constraints, researchers have devised a cost-effective and environmentally sustainable approach known as the utilization of plant extracts for the synthesis of nanoparticles, which involves a single-step process [23]. The presence of dyes in industrial effluent can have significant adverse effects on the environment and pose risks to both human health and aquatic organisms.

The degradation of the organic pollutants present in wastewater might be achieved by the process of photocatalysis, which involves the use of metal oxide semiconductor nanostructures [24]. Photocatalysts are a class of semiconductors that possess the ability to enhance reaction rates upon exposure to photons while remaining unchanged in their own chemical composition [25]. Common examples of semiconductor photocatalysts are titanium dioxide (TiO_2), zinc oxide (ZnO), iron(III) oxide (Fe_2O_3), zinc sulfide (ZnS), and cadmium sulfide (CdS) [26]. These semiconductors exhibit a full valence band and an unfilled conduction band [27]. Sunlight-driven catalysis has emerged as a promising method for wastewater purification due to its environmentally friendly nature, cost-effectiveness, simplicity of operation, and high efficacy [28]. An ideal photocatalyst should possess a very broad absorption spectrum, ideally including the visible or near-ultraviolet regions of the electromagnetic spectrum [29]. The presence of an adequate number of electron-unoccupied states is necessary to impede the recombination of electron–hole pairs generated from the bombardment of photons [30]. Several studies have reported different environmental applications for photocatalysts. A previous study proposed a straightforward approach for the controlled production of FeNiV oxides with high-valence Mo modifications, which serve as effective catalysts for the oxygen evolution reaction (ORE). The investigation determined that the incorporation of Mo has a notable impact on the valence state of Fe species within the catalysts, resulting in adjustable OER performance [31]. In addition, the utilization of Ta_3N_5/CdS nanofibers demonstrates exceptional efficacy in the breakdown and mineralization of tetracycline via photocatalytic processes. Furthermore, these

nanofibers exhibit a high degree of efficiency in the reduction of hexavalent chromium Cr(VI) via photocatalysis [32]. Another study has shown that BiOBr/ZIF-67 nanocomposites on carbon fiber cloth (CFC) has been employed as a filter membrane for the purpose of the photocatalytic elimination of contaminants in continuously running wastewater [33]. A previous study demonstrated a novel approach in the design of carbon dots involving the creation of S-scheme heterostructures. This strategy aims to simultaneously enhance the anti-photo-corrosion performance and strengthen the photocatalytic performance of sulfides, therefore achieving two objectives with a single method [34]. Gadolinium-doped two-dimensional bismuth molybdate nanosheets have been shown to exhibit photocatalytic activity for efficient nitrogen reduction in another study [35]. The present study was conducted to examine the utilization of iron oxide nanoparticles synthesized using environmentally friendly methods for the purpose of removing crystal violet dye. This research aims to establish a cost-effective and environmentally sustainable approach for the purification of polluted water. Furthermore, an assessment was conducted to evaluate the antioxidant and antifungal properties of the biosynthesized IONPs.

2. Materials and Methods

2.1. Preparation of the Plant Extract

Camellia sinensis var. sinensis leaves were procured at a nearby marketplace in Riyadh, Saudi Arabia. The identification of the plant specimens was confirmed by the herbarium located within the department of Botany and Microbiology. The dried *C. sinensis* leaves underwent a triple purification process involving the use of distilled water following an initial washing with tap water. Subsequently, they were left in shade to achieve complete dryness. Afterwards, the leaves were pulverized into a fine homogeneous powder using a mechanical blender. A 500 mL flask was utilized to accommodate a quantity of 50 g of plant powder together with 200 mL of distilled water. The flask was exposed to a temperature of 60 °C for 30 min using a hot plate. The flask was thereafter subjected to continuous agitation for a period of 24 h at 25 °C, assisted by the use of a magnetic stirrer. Subsequently, the combination was subjected to purification using Whatman filter paper (1) to acquire of a refined filtrate and eliminate any residual contaminants. Following this, the extract was subjected to sterilization via filtration using a 0.45 µm Millipore membrane filter. Following this, the produced extracts were refrigerated at 4 °C to preserve them for future experiments.

2.2. Green Fabrication of the Phytosynthesized IONPs

For the process of synthesizing iron oxide nanoparticles (IONPs), a solution consisting of 0.01 M ferric nitrate ($Fe(NO_3)_3.9H_2O$) was combined with the aqueous *C. sinensis* leaf extract in a 1:1 proportion. The formation of a black color indicated the potential development of IONPs. The reaction mixture underwent centrifugation at 10,000 rpm for 10 min. After the centrifugation procedure, the supernatant was extracted and then disposed of. The pellets were subjected to a triple washing procedure with distilled water to effectively remove any contaminants [36].

2.3. Characterization of the Biogenic IONPs

2.3.1. UV Optical Spectroscopy

The biogenic IONPs were first distributed in distilled water and their absorbance within the wavelength range of 200–800 nm was then measured using a UV-VIS-NIR spectrophotometer (UV-1601, Shimadzu, Kyoto, Japan). The blank solution used in the experiment was composed of distilled water.

2.3.2. Transmission Electron Microscopy (TEM) Analysis

The biogenic IONPs underwent an initial triple washing process using deionized water. The specimens were positioned on a copper grid that had been covered with a layer of carbon, then removed and subjected to a drying process prior to analysis. A transmission

electron microscope (JEOL, JEM1011, Tokyo, Japan) was used to conduct the analysis at the Electron Microscope Unit of the College of Science at King Saud University. The TEM test was used to observe and analyze the morphological characteristics and particle size distributions of the IONPs. This technique generated high-resolution two-dimensional pictures at a voltage of 100 kV.

2.3.3. Energy Dispersive X-ray (EDX) Analysis

The elemental composition of the biogenic IONPs was determined via the use of a scanning electron microscope (SEM) equipped with an energy dispersive X-ray (EDX) analyzer (JEOL, JSM-6380 LA, Tokyo, Japan).

2.3.4. FTIR (Fourier Transform Infrared) Analysis

The surface chemistry of the produced IONPs was analyzed using FTIR spectroscopy. The identification of the functional groups present on the surface of the nanoparticles was accomplished by analyzing the infrared absorption frequencies. The sample preparation process included the dispersion of IONPs inside a dry KBr matrix. Subsequently, the mixture was compressed to create a visually clear disc. A KBr pellet was used as a reference standard.

2.3.5. XRD Analysis

The X-ray powder diffraction (XRD) patterns were obtained using a Shimadzu XRD model 6000 diffractometer (Shimadzu, Columbia, SC, USA) equipped with a graphite monochromator and Cu-K radiation. A step-scanning program was used to conduct an XRD analysis on a film composed of biosynthesized IONPs. The software (Version 5.921) utilized a step size of 0.02 per step, and each step had an acquisition length of 5 s at a 2-theta angle. The crystalline phases were identified using the Joint Committee on Powder Diffraction Standards (JCPDS).

2.3.6. Brunauer–Emmett–Teller (BET)/Barrett–Joyner–Halenda (BJH) Analysis

A combined BET and BJH analyzer (Automated Gas Sorption Analyzer, Model Nova Station A, Quatachrome Instrument, Boynton Beach, FL, USA) was utilized for the determination of the specific surface area, pore size, and pore volume of the biogenic IONPs.

2.3.7. Zeta Potential Analysis

The biosynthesized IONPs were characterized by measuring their zeta potential and dynamic light scattering (DLS) using a zeta sizer device (Malvern Instruments Ltd.; zs90, Worcestershire, Malvern, UK).

2.4. Photoctalytic Degradation of Synthetic Dyes Using IONPs

The assessment of the crystal violet dye degradation was conducted by examining different concentrations of iron oxide nanoparticles (0.125, 0.250, 0.5, and 1.0 mg mL^{-1}) and varying contact durations (30.0, 60.0, 90.0, 120.0, 150.0, 180.0, and 210.0 min). The percentage of decolorization in response to sunlight was assessed at an average sunlight irradiation of 1000 W/m^2 at 38 ± 2 °C and also under dark conditions. In order to establish the adsorption/desorption equilibrium state, a solution containing 10 mg L^{-1} of crystal violet dye and a concentration the biogenic IONPs was subjected to continuous swirling for a duration of 30 min prior to the commencement of the photocatalytic experiment. The total volume of the solution used was 100 mL. The effectiveness of the decolorization was assessed using the following methodology: A volume of 1.0 mL was extracted from each treatment and subjected to centrifugation at 10,000 rpm for 3.0 min. The resulting samples were then analyzed for optical density (OD) at a wavelength corresponding to the maximum absorption band (λ_{max}) of the crystal violet dye solution, namely 588 nm. This measurement was performed using a spectrophotometer (model 721, manufactured

by M-ETCAL). The decolorization percentage (%) of the crystal violet dye was calculated using the following formula:

The decolorization percentage (D (%)): [dye (i) − dye (f)/dye (i)] × 100, where dye (i) represents the initial absorbance and dye (f) represents the final absorbance observed at various time intervals.

2.5. Determination of Photocatalysis Reaction at Different pH Values

The decolorization percentages of the crystal violet dye at pH values of 2, 3, 4, 5, 6, 7, 8, and 9 were evaluated to detect the optimum conditions for a photocatalysis reaction. The biogenic IONPs (1.0 mg/mL) were investigated for their photocatalytic activity at different pH values under sunlight irradiation of 1000 W/m^2 for about 210 min at 38 ± 2 °C. The reaction conditions were adjusted as described previously and the decolorization percentages of the crystal violet dye were calculated at different pH values.

2.6. Cycling Test of the Biogenic IONPs

The biogenic IONPs were separated from the dye solution, dispersed in distilled water for 2 h, and then removed, dried overnight, and reused in a second cycle for the adsorption of the crystal violet dye. Thereafter, the adsorbents were utilized five additional times. A UV-visible spectrophotometer was used to determine the remaining dye concentration at 580 nm. The adsorption percentage was determined according to the following equation:

$$\text{Adsorption } \% = \frac{C_0 - C_t}{C_0}$$

where C_0 and C_t are the CV concentrations (mg/L) before and after adsorption, respectively.

2.7. Antioxidant Assay

The efficiency with which the biogenic IONPs scavenged free radicals was evaluated via the implementation of a 1,1-diphenyl-2-picrylhydrazyl (DPPH) test. Various concentrations (50, 100, 150, 200, and 250 mg/mL) of the biogenic IONPs were adjusted by dissolving them in methanol. A 1 mM solution of DPPH was made by dissolving it in 100 mL of methanol. A 2 mL DPPH solution was combined with biogenic iron oxide nanoparticles of different concentrations. The solutions underwent incubation at room temperature for 30 min in the absence of light. In this study, ascorbic acid was employed as the positive control, while an equal quantity of methanol and DPPH was used as the blank. The measurement of absorbance at a specific wavelength of 517 nm was conducted using a UV spectrophotometer to determine the extent of inhibition in the reaction mixtures. The inhibition percentage was then determined using the following equation:

$$\% \text{ DPPH scavenging} = [(A - B)/A] \times 100$$

The absorbance of the control is denoted as A, whereas the absorbance of the sample is denoted as B.

2.8. Statistical Analysis

The data from the present investigation were subjected to analysis using GraphPad Prism version 8.0 (GraphPad Software, Inc., La Jolla, CA, USA) via a Tukey test of one-way ANOVA with a significance level of 0.05. The results are reported in the form of the mean of triplicates ± standard error.

3. Results and Discussion

3.1. Green Synthesis of Bioinspired IONPs

The bioinspired IONPs were synthesized using a water extract derived from the *C. sinensis* leaves. The results presented in Figure 1 demonstrate the utilization of the prepared extract to reduce the ferric nitrate solution, resulting in the generation of bioinspired

IONPs. The formation of a black color in the solution indicated the successful development of the IONPs. The composition of the water extract from the *C. sinensis* leaves was determined using gas chromatography–mass spectrometry (GC-MS) in a previous investigation. The analysis revealed the presence of caffeine, catechol, 1,2,3-benzenetriol, 1,3,5-benzenetriol, 6-Hydroxy-4,4,7a-trimethyl-5,6,7a-tetrahydrobenzofuran, 1,1′-Biphenyl, 2-ethyl-, and methoxy resorcinol [37]. It was hypothesized that these phytoconstituents found in the green tea extract functioned as reducing agents for the ferric nitrate solution, and also as biostabilizing and capping agents. The bioprepared IONPs were characterized using different physicochemical techniques to detect their different physical and chemical features.

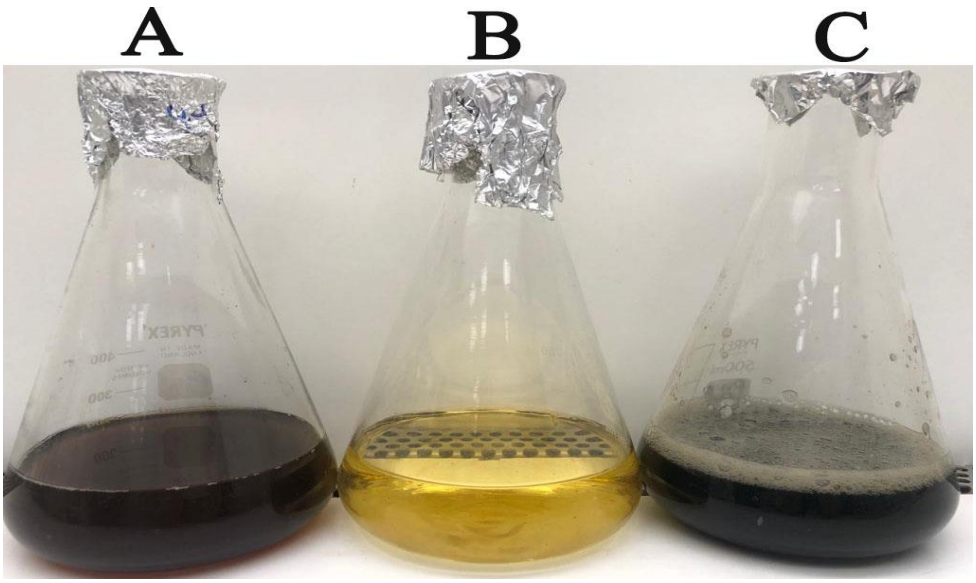

Figure 1. Green fabrication of IONPs using aqueous *C. sinensis* extract. (**A**) Water extract of *C. sinensis* leaves; (**B**) ferric nitrate solution; (**C**): bioinspired IONPs.

3.2. UV Analysis of the Bioinspired IONPs

The emergence of a black-colored solution is attributed to the surface plasmon resonance (SPR) vibrations of the bioinspired IONPs. The process by which the IONPs were synthesized was observed using UV-visible spectroscopy. The UV-visible spectra of the synthesized IONPs exhibited a distinct peak at 241 nm, which may be attributed to SPR vibrations occurring inside the reaction mixture (Figure 2). The findings of our study align with those of a previous publication that reported the presence of a UV peak at 254 nm, which can be attributed to the SPR vibrations of the biogenic IONPs synthesized using an extract derived from *Solanum lycopersicum* leaves [36]. According to a previous study by Mirza et al. (2018), the presence of a distinctive absorbance peak at around 250 nm in the UV spectrum is a distinguishing property of IONPs [38]. The diffuse reflectance spectroscopy (DRS) technique can very efficiently determine the reflectance properties of powdered samples [39]. In this context, the findings revealed a strong absorption band within the visible light spectrum (400–800 nm), with a discernible peak seen at 475 nm (Figure 3). This observation suggests that the biogenic IONPs can potentially be used in photocatalytic reactions because their UV band falls between 400 and 800 nm in the visible light range [35,40]. The band gap energy of the biogenic IONPs was found to be 2.6 eV using Planck's equation, $Eg = hc/\lambda$, where c is the speed of light = 3.0×10^8 m s^{-1}, h is the Planck constant (4.136×10^{-15} eV s), and λ is the wavelength (475×10^{-9} m). The calculated band gap energy was matched with those of prior studies which reported the photocatalytic activities of iron oxide nanoparticles [41,42].

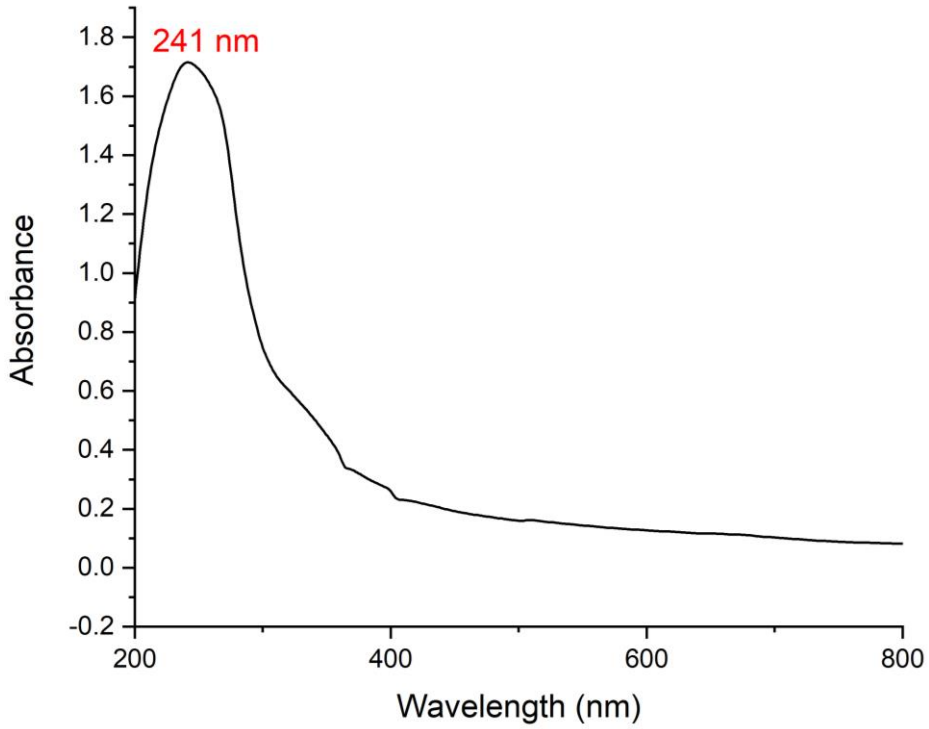

Figure 2. UV-vis spectrum of the biogenic IONPs.

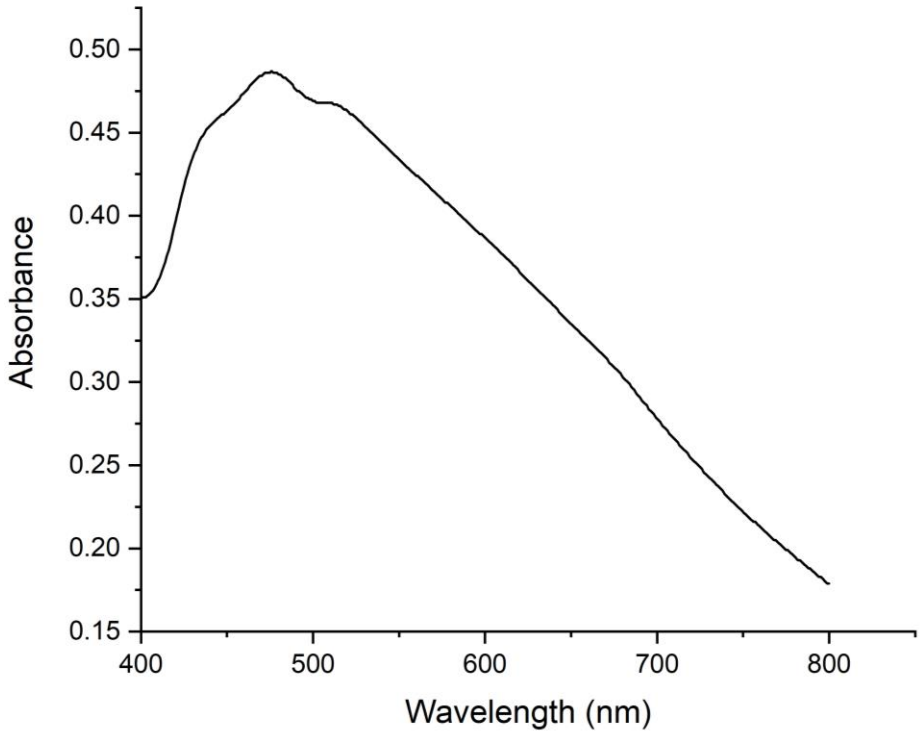

Figure 3. DRS of the powdered biogenic IONP sample.

3.3. EDX Analysis of the Biogenic IONPs

The EDX analysis of the bioinspired IONPs demonstrated the presence of iron peaks at energy levels of 0.8, 6.4, and 7.0 keV corresponding to the Fe La, Fe Ka, and Fe Kb signals, respectively. The analysis revealed that the sample included an iron mass percentage of 86.51% (Figure 4). This finding suggests that the utilization of *C. sinensis* leaf extract in

the biosynthesis process is highly efficient. The detected carbon peak at 0.3 keV could be attributed to the carbon holder bearing the IONP sample [38].

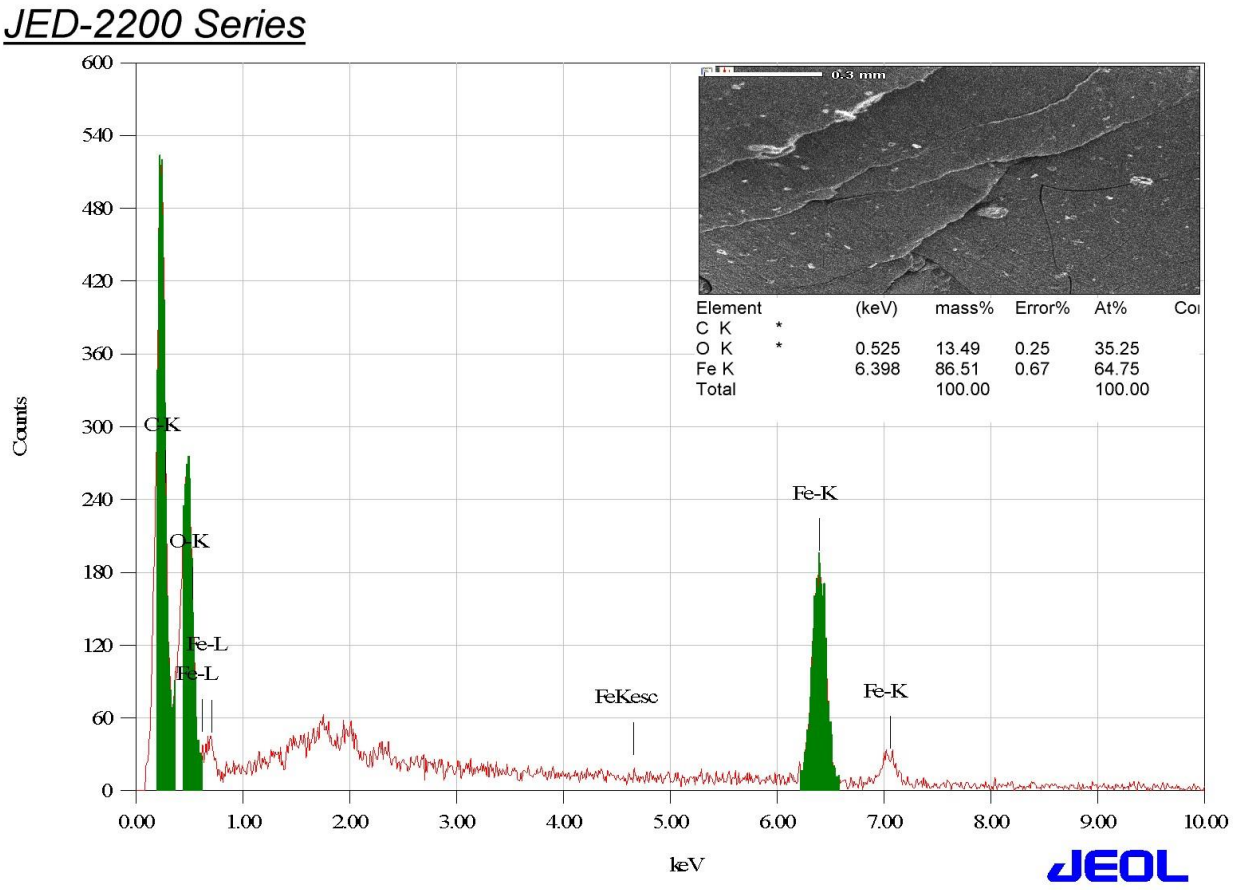

Figure 4. Elemental composition of the bioinspired IONPs.

3.4. FTIR Analysis of the Biogenic IONPs

A FTIR analysis was conducted to detect the main functional groups of the bioinspired IONPs. The FTIR spectra revealed the presence of eight diffraction peaks at 3308.89, 2182.76, 2142.54, 1989.87, and 1636.93 cm^{-1} (Figure 5). The broadband recorded at a wavenumber of 3308.89 cm^{-1} in the spectrum of the *C. sinensis* extract may be attributed to the stretching of the O-H bonds in the alcohols and phenols [43]. Similarly, the wide band seen at a wavenumber of 3344.26 cm^{-1} in the spectrum of the biogenic IONPs might be attributed to the stretching of the O-H bonds in the phenolic compounds, suggesting the presence of polyphenolic compounds that act as capping agents on the biosynthesized IONPs. The band detected at 2182.76 cm^{-1} in the spectrum of the biogenic IONPs was shifted to 2205.74 cm^{-1} and attributed to C≡C stretching of alkynes (Table 1) [44]. Furthermore, the absorption bands seen at a wavenumber of 1636 cm^{-1} in the spectrum of the biogenic IONPs and the *C. sinensis* extract might be attributed to the bending motion of the C=C stretching in the alkenes [45]. On the other hand, the bands detected at 2171.27 and 2023.52 cm^{-1} in the spectrum of the biogenic IONPs might be attributed to the presence of thiocyanate and isothiocyanate compounds [46]. However, the band detected at 1989.87 cm^{-1} in the spectrum of the biogenic IONPs could be attributed to the C-H bending of the aromatic compounds.

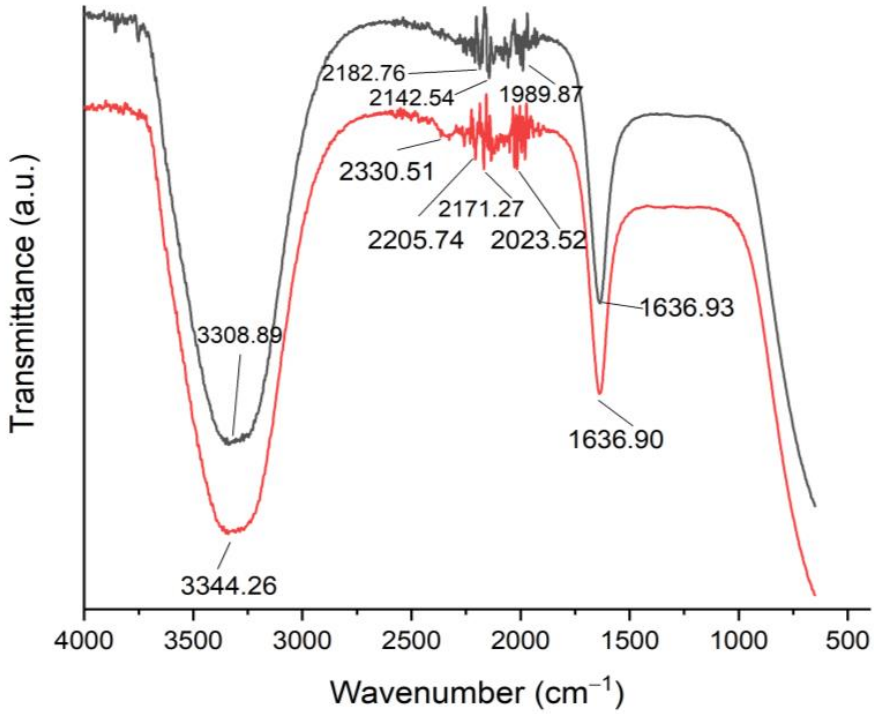

Figure 5. FTIR spectra of *C. sinensis* extract and biogenic IONPs (Black line represent FTIR spectrum of *C. sinensis* extract; Red line represent FTIR spectrum of the biogenic IONPs).

Table 1. Functional groups of biogenic IONPs and *C. sinensis* extract.

Functional Groups of *C. sinensis* Extract				
No.	**Absorption Peak (cm^{-1})**	**Appearance**	**Functional Groups**	**Molecular Motion**
1	3308.89	Strong, broad	Alcohols and phenols	O-H stretching
2	2182.76	weak	Alkynes	C≡Cstretching
3	2142.54	weak	Thiocyanate	S-C≡N stretching
4	1989.87	weak	Aromatic compound	C-H bending
5	1636.93	Medium	Alkenes	C=C stretching
Functional groups of biogenic IONPs				
1	3344.26	Strong, broad	Alcohols and phenols	O-H stretching
2	2330.51	Weak	Carbon dioxide	O=C=O stretching
3	2205.74	Weak	Alkynes	C≡Cstretching
4	2171.27	Weak	Thiocyanate	S-C≡N stretching
5	2023.52	Weak	Isothiocyanate	N=C=S stretching
6	1636.90	Medium	Alkenes	C=C stretching

3.5. TEM Investigation of the Bioinspired IONPs

To determine the size, form, and particle size distribution of the bioinspired IONPS, a TEM examination was performed. As can be seen in Figure 6, the phytosynthesized IONPs were found to be spherical in shape and enclosed inside a matrix-like structure that might be attributed to the capping agents of the phytomolecules of the *C. sinensis* leaf extract used in the biosynthesis process. Figure 7 shows that the average diameter of the FeONPs was 49.63 ± 9.23 nm.

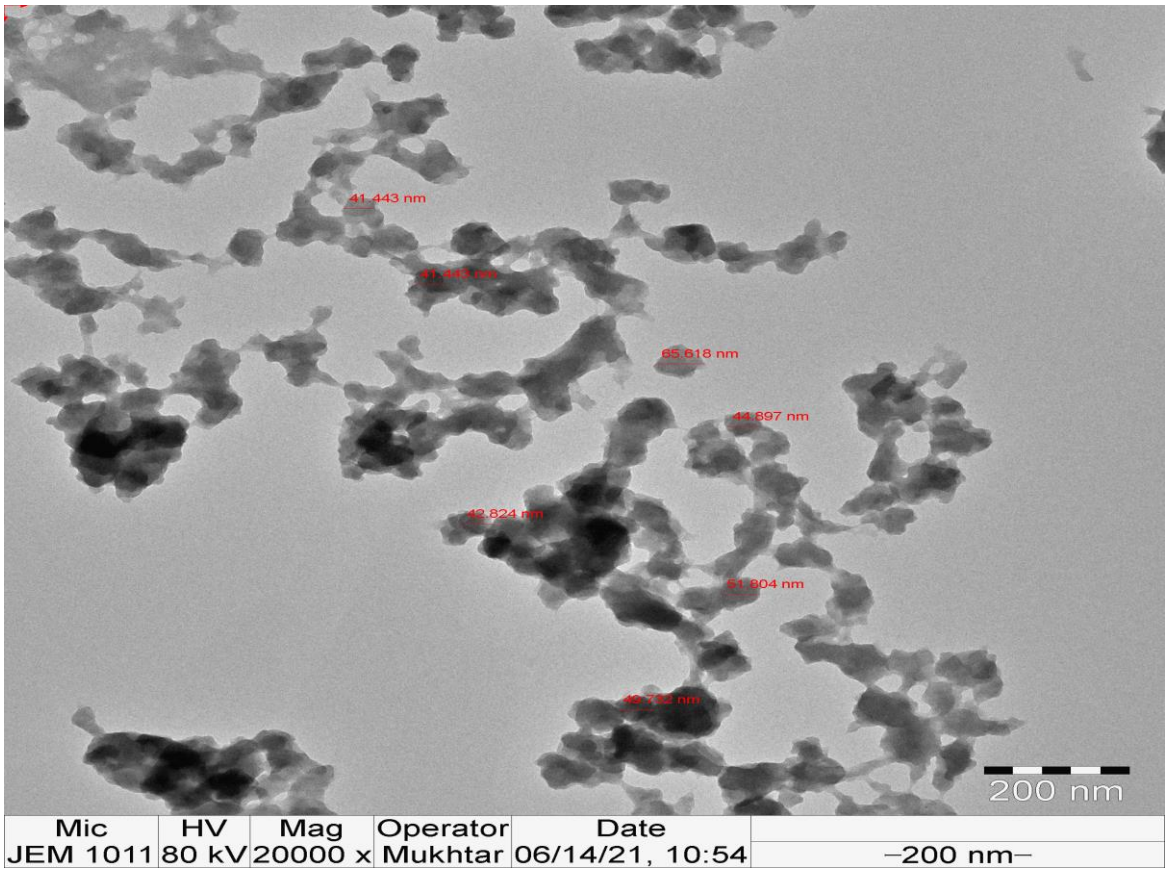

Figure 6. TEM micrographs of the phytosynthesized IONPs.

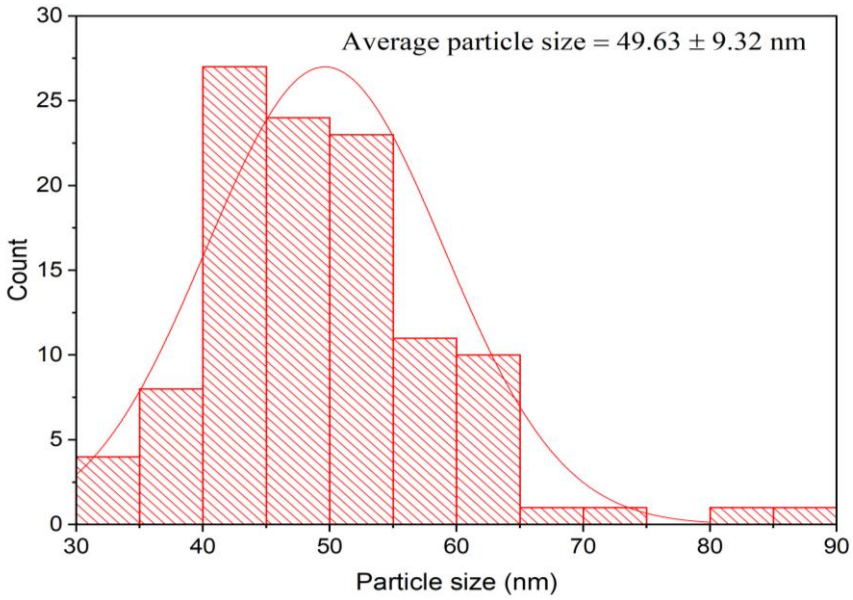

Figure 7. Particle size distribution histogram of the bioinspired IONPs.

3.6. XRD Analysis of the Biogenic IONPs

The X-ray diffraction (XRD) pattern of the biogenic IONPs derived from the green tea extract was examined in order to gain a deeper understanding of the crystalline structures of the synthesized nanomaterials in their original state. As can be seen in Figure 8, the XRD pattern lacks discernible diffraction peaks, indicating that the synthesized IONPs possess an amorphous structure. Our findings align with those of prior reports that have

demonstrated the amorphous forms of the biosynthesized IONPs [47,48]. Iron oxides may be found in nature in either amorphous or crystalline states [49]. Among the several crystalline forms, magnetite (Fe_3O_4), maghemite (γ-Fe_2O_3), and hematite (α-Fe_2O_3) are the most prevalent phases of iron oxides. Both the crystalline and amorphous forms of iron oxides exhibit distinct characteristics that enable their use in many sectors [50].

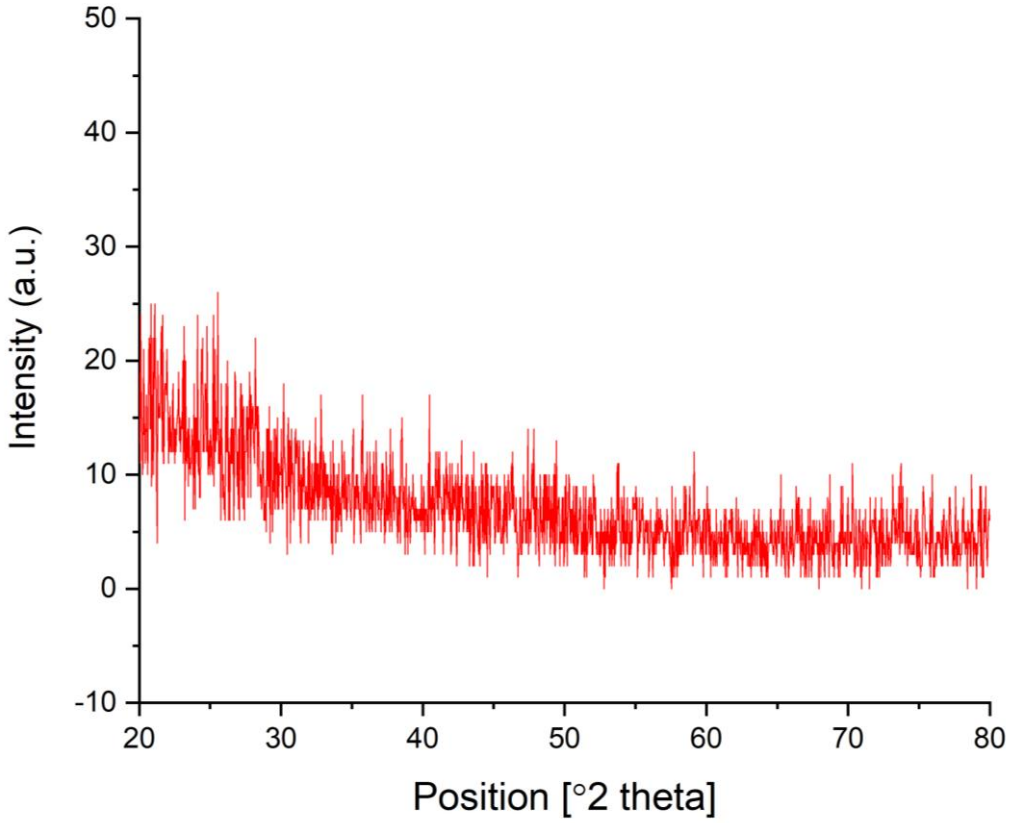

Figure 8. XRD pattern of the bioinspired IONPs derived from the *C. sinensis* leaf extract.

3.7. Specific Surface Area, Pore Size, and Pore Volume of the Biogenic IONPs

Advanced applications require amorphous IONPs that possess a very large surface area as opposed to iron oxides with crystal structures that have well defined features [51]. Amorphous metal oxides have significance in several industrial fields, such as electronics, solar energy conversion, catalysis, magnetic storage device manufacturing, and electrochemistry, as well as adsorption and decontamination procedures [52]. These applications exclusively employ amorphous IONPs owing to their exceptional catalytic characteristics, superparamagnetism, and larger surface area [53]. The biogenic IONPs were found to have a specific surface area of 48.49 m^2/g, as shown in Table 2. Additionally, the pore size of these nanoparticles was found to be 1.74 nm, while the specific pore volume was determined to be 0.031 cm^3/g. Our results were in accordance with those of a prior study which demonstrated the biosynthesis of magnetite nanoparticles of a specific surface area measuring 47.07 m^2/g synthesized using *Peltophrorum pterocarpus* extract [54]. Moreover, the results of the present study are consistent with those of a previous study that showcased the environmentally friendly production of amorphous IONPs with a precise surface area of 46.6 m^2/g produced using an extract derived from the leaves of *Prosopis Africana* [55]. A previous study showed that the ability to adsorb CO_2 can be significantly enhanced by using magnetite nanoparticles as a surface decoration on multiwalled carbon nanotubes. The magnetite nanoparticles exhibited a pore size ranging from 1.7 to 2.5 nm, which aligns with the results obtained in our study [56]. A prior investigation documented the 0.0222 cm^3/g pore volume of α-Fe_2O_3 nanoparticles which were synthesized utilizing a *Spondias dulcis* leaf extract [57]. Collectively, the findings of the current study affirm that the biosynthesized

IONPs possessed a high surface area and a microporous nature. These characteristics have been reported to enhance the photocatalytic and adsorptive activities of biogenic IONPs when used in dye removal and various environmental applications [58].

Table 2. Specific surface area, pore size, and pore volume of the biogenic IONPs.

Parameter	Value
Specific surface area (m^2/g) BET	48.3
pore size (nm) BJH	1.74
pore volume (cm^3/g) BJH	0.022

3.8. Zeta Potential Analysis

A zeta potential analysis of the bioinspired IONPs was conducted to investigate their surface charge, and the dynamic light scattering showed the average hydrodynamic diameter of the colloidal nanoparticles. It was observed that the average hydrodynamic diameter of the bioinspired IONPs was 655 nm (Figure 9), a value notably larger than that obtained through the TEM analysis. This disparity can be attributed to the fact that the TEM technique measures the diameter of both the biogenic IONPs and the capping molecules surrounding them, as evidenced by the TEM micrographs, as well as the additional hydrate layers enveloping the bioinspired IONPs [59]. However, the surface charge of the bioinspired IONPs was −5.69 mV (Figure 10). The observed negative surface charge of the bioinspired IONPs might be attributed to the presence of capping biomolecules derived from the extract used in the biosynthesis. The stability of nanoparticles is influenced by many parameters, including the physicochemical properties of the solvent, the extract, electrostatic interactions, and van der Waals forces [60]. The inclusion of hydroxyl (OH) functional groups on the surface of the iron oxide nanoparticles was shown to be crucial in generating negative charges on the nanoparticles [61]. The biogenic IONPs possessed a negative surface charge, which we attribute to the presence of capping molecules from the extract. This observation indicates that the biosynthesized nanoparticles exhibited repulsive forces which contributed to their colloidal stability [62].

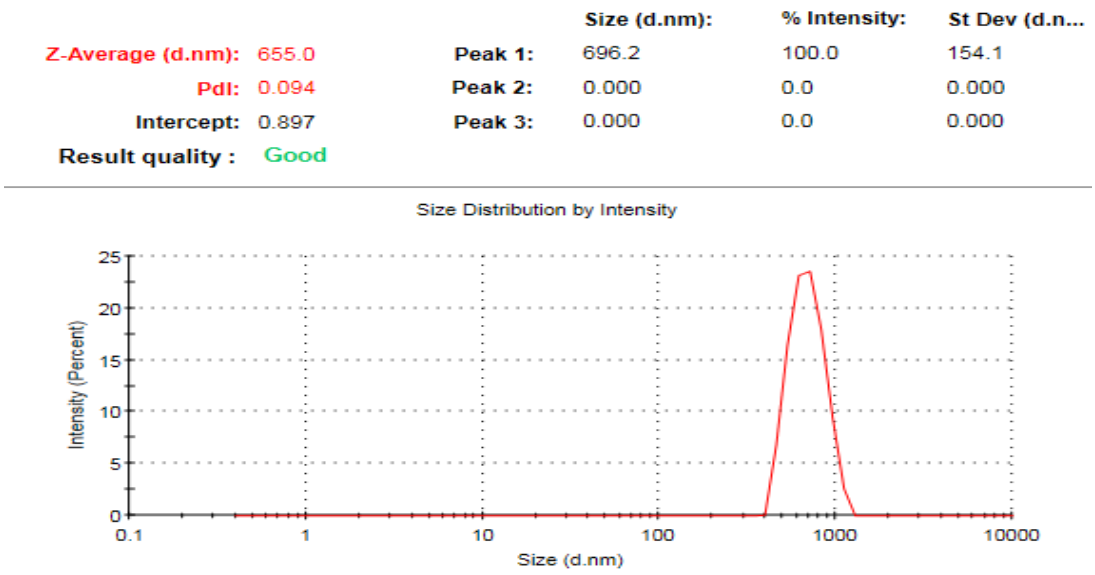

Figure 9. The average hydrodynamic diameter of the biogenic IONPs.

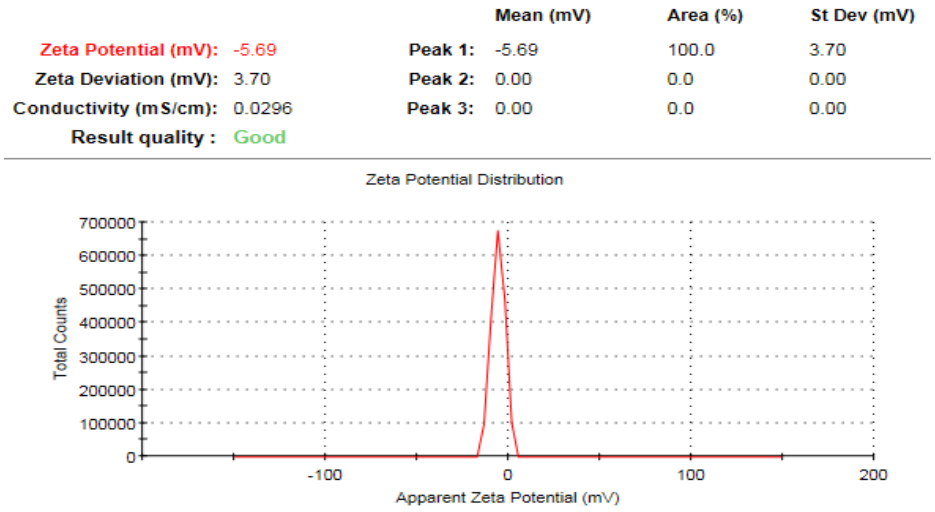

Figure 10. The surface charge of the phytosynthesized IONPs.

3.9. Photocatalytic Degradation of Crystal Violet Dye Using IONPs

Nanoparticles are subjected to irradiation using a light source, and the degradation process encompasses two approaches: the direct exposure of the nanomaterial surfaces to high-energy light sources, or the implementation of a photosensitization method [63]. In the context of direct photocatalytic degradation, the phenomenon of photoexcitation arises, in which electrons are transitioned from the valence band (occupied) to the conduction band via the absorption of light energy [64]. The decolorization of the crystal violet dye was investigated using biogenic IONPs at different concentrations (0.25, 0.5, 0.75, and 1.0 mg mL^{-1}) and at different time intervals (30.0, 60.0, 90.0, 120.0, 150.0, 180.0, and 210.0 min) under sunlight and dark conditions. The photocatalytic activity of the bioinspired IONPs was time and concentration dependent. The bioinspired IONPs exhibited their maximum photocatalytic activity at a concentration of 1 mg/mL, resulting in relative decolorization percentages ranging from 36.17% to 99.23% at reaction durations of 30 and 210 min, respectively. Nevertheless, the biogenic IONPs exhibited their lowest levels of decolorization when subjected to sunlight reactions at a concentration of 0.125 mg/mL. The recorded decolorization percentages varied from 4.78% to 27.16% (Figure 11A). At a concentration of 0.250 mg/mL of biogenic IONPs, the decolorization percentages ranged from 12.52% to 61.53% over respective experimental periods of 30 to 210 min under sunlight conditions (Figure 11B). Moreover, the biogenic IONPs at a concentration of 0.50 mg/mL revealed decolorization percentages ranging from 31.56 to 82.68% at reaction times of 30 and 210 min, respectively, under sunlight conditions (Figure 11C). Under dark conditions, the highest decolorization percentage of the crystal violet dye was detected at a concentration of 1.0 mg/mL, and a relative decolorization percentage of 64.23% was recorded at a reaction time of 210 min (Figure 11D). In the presence of a photocatalyst, the generation of surface plasmons by the nanoparticles occurred via echoing stimulation through the molecular system [65]. Hence, the initiation of the dye degradation was facilitated by the creation of photonic stimulation by the nanoparticles [66]. The increased surface area of the IONPs facilitated the generation of hydroxyl radicals, which promoted the breakdown of the crystal violet dye. The photocatalytic degradation of indigo carmine dye under sunlight irradiation utilizing biogenic IONPs synthesized using *Azadirachta indica* leaf extract was reported in a study conducted by Muthukumar et al. [67]. In a recent study conducted by Bishnoi et al., the degradation of methylene blue dye utilizing IOPNs that were synthesized using a fruit extract derived from *Cynometra ramiflora* was reported [68]. The findings of our current investigation demonstrate that the biogenic IONPs synthesized using *C. sinensis* leaf extract exhibit significant photocatalytic activity against crystal violet dye, which aligns with previous reports.

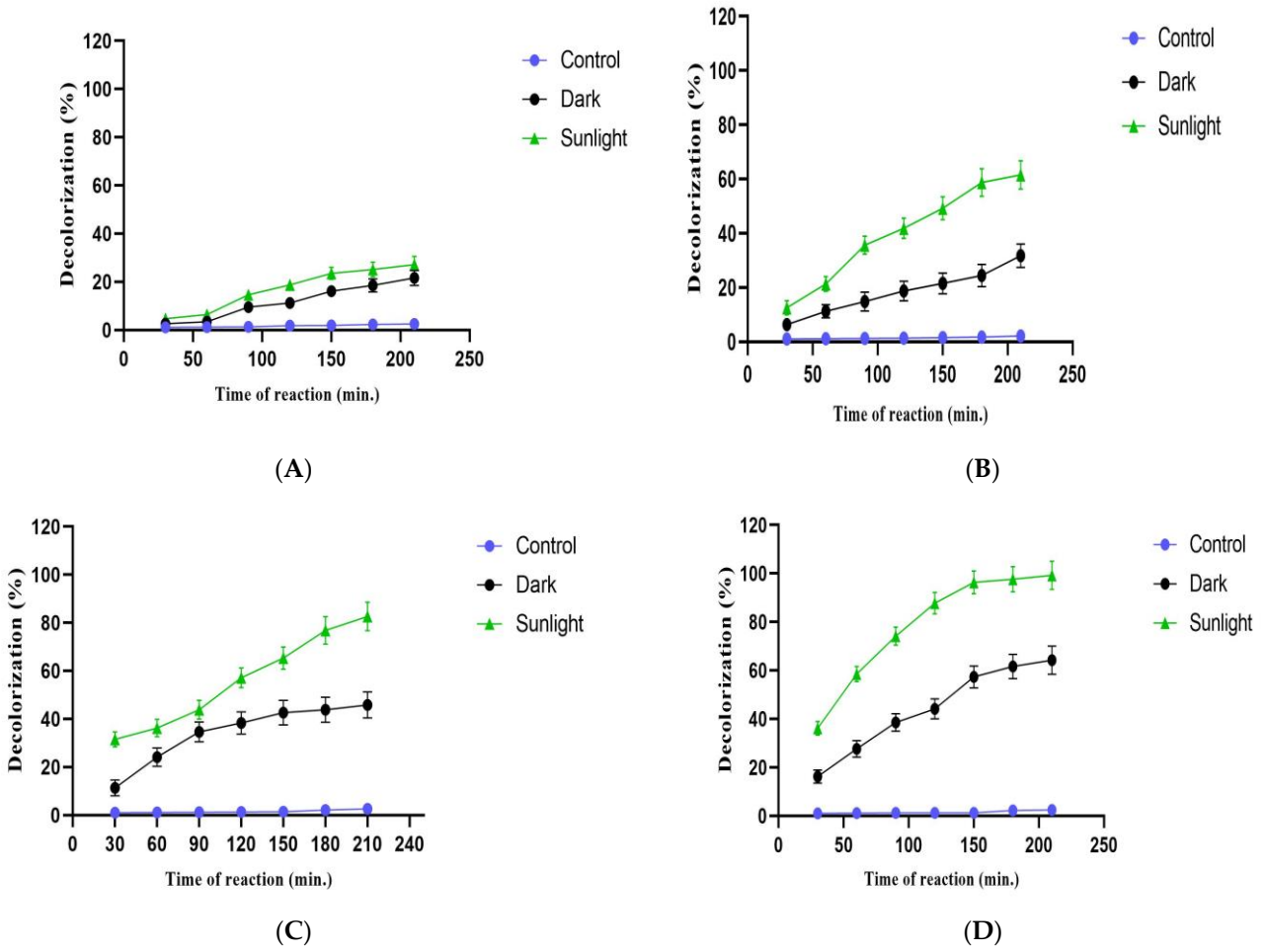

Figure 11. Decolorization percentages of crystal violet dye at different time intervals and different biogenic IONP concentrations. (**A**) Decolorization percentages at an IONP concentration of 0.125 mg/mL; (**B**) decolorization percentages at an IONP concentration of 0.250 mg/mL; (**C**) decolorization percentages at an IONP concentration of 0.50 mg/mL; (**D**) decolorization percentages at an IONP concentration of 1.0 mg/mL.

The adsorption percentages of the biogenic IONPs (1.0 mg/mL) under dark and sunlight conditions at different time intervals are presented in Table 3. The decolorization percentage was significantly increased from 36.17 to 99.23% under sunlight irradiation at 30 and 210 min, respectively. The results of the present study have confirmed the considerable photocatalytic efficacy of the biogenic IONPs when exposed to sunlight, which enables the efficient elimination of crystal violet dye. In contrast, the biogenic IONPs exhibited reduced adsorption efficacy in the absence of light, under which conditions the relative adsorption percentages varied from 16.24% to 64.23% after 30 and 210 min, respectively.

3.10. Detection of Photocatalytic Activity of the Biogenic IONPs at Different pH Values

The photocatalytic performance of the biogenic IONPs was assessed under several pH values in order to identify the optimal parameters for the photocatalytic process. The biogenic IONPs exhibited their maximum photocatalytic activity at pH values of 6, 8, and 9. This was shown by the respective relative decolorization percentages of 98%, 99.1%, and 99.6%, which are shown in Figure 12.

Table 3. Decolorization percentages of crystal violet dye under sunlight and dark conditions at different time intervals and an IONP concentration of 1.0 mg/mL.

Reaction Time (min.)	Decolorization Percentages (%)	
	Sunlight	Dark
30	36.17	16.24
60	58.54	27.63
90	74.12	38.54
120	87.76	44.17
150	96.32	57.32
180	97.63	61.63
210	99.23	64.23

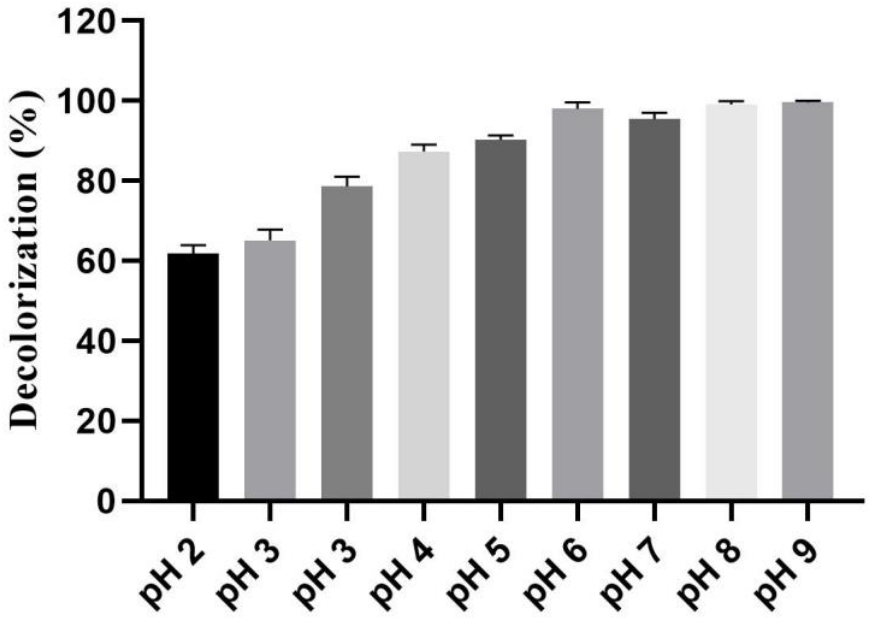

Figure 12. Effect of different pH values on the photocatalysis reaction.

3.11. Cycling Test of the Biogenic IONPs

A cycling test of the biogenic IONPs demonstrated that their adsorption percentage slightly decreased from 91.05 to 77.41% after five cycles (Figure 13). This finding provides clear evidence of the potential reusability of the biogenic IONPs. However, it is worth noting that the slight decrease in observed adsorption percentages may be attributed to the washing process, which has the potential to reduce adsorption efficiency [69]. Additionally, it is possible that some of the adsorption sites may become denatured or covered by pollutants, leading to a decrease in overall adsorption efficiency [70]. Figure 14 shows an SEM image of the sample after the cycling test showed the presence of nanoparticles with increased size due to the adsorption of the crystal violet dye by the biogenic IONPs, which led to the clumping and aggregation of the nanoparticles together.

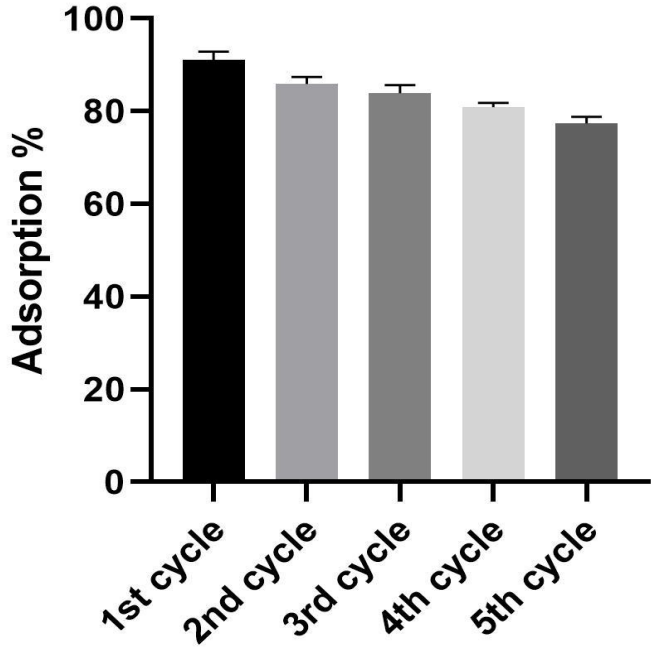

Figure 13. Regeneration efficiency of the biogenic IONPs.

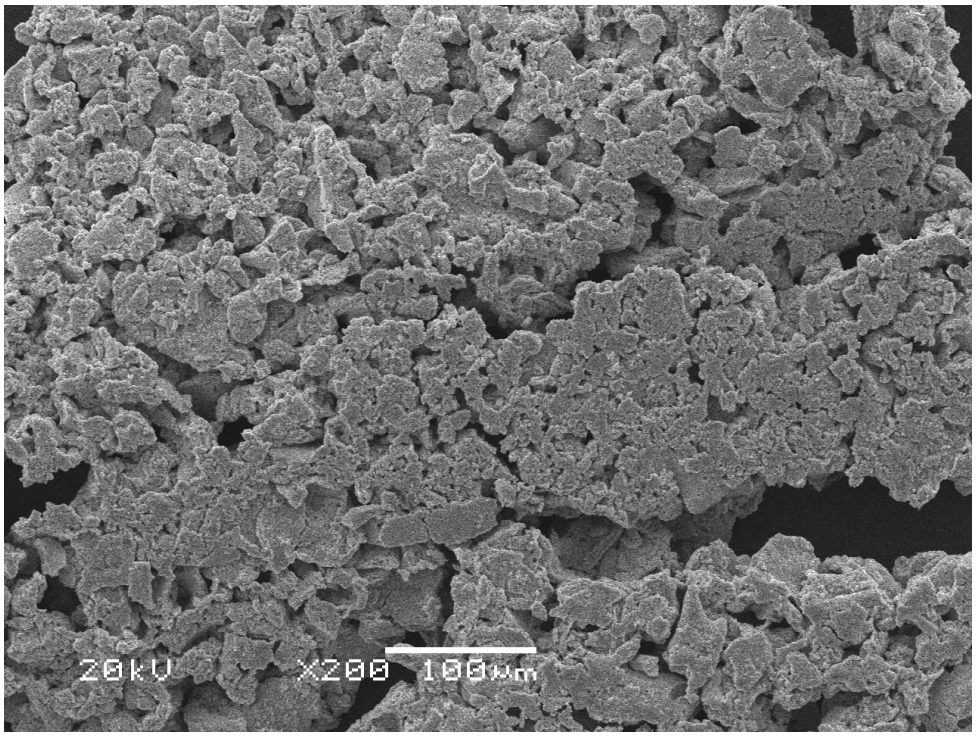

Figure 14. SEM image of the biogenic IONPs after a cycling test.

3.12. Antioxidant Activity

The DPPH inhibition percentages of the biogenic IONPs synthesized using the *C. sinensis* leaf extract were determined at concentrations ranging from 20 to 100 μg/mL. The results showed that the inhibition percentages varied from 21.45% to 74.69%, respectively (Figure 15). The DPPH inhibition percentages of the ascorbic acid varied from 26.14% to 76.48% across doses ranging from 20 to 100 μg/mL, respectively. Furthermore, the determined IC_{50} value of the biogenic IONPs was 64.31 μg/mL, while the standard ascorbic acid exhibited an IC_{50} of 56.87 μg/mL.

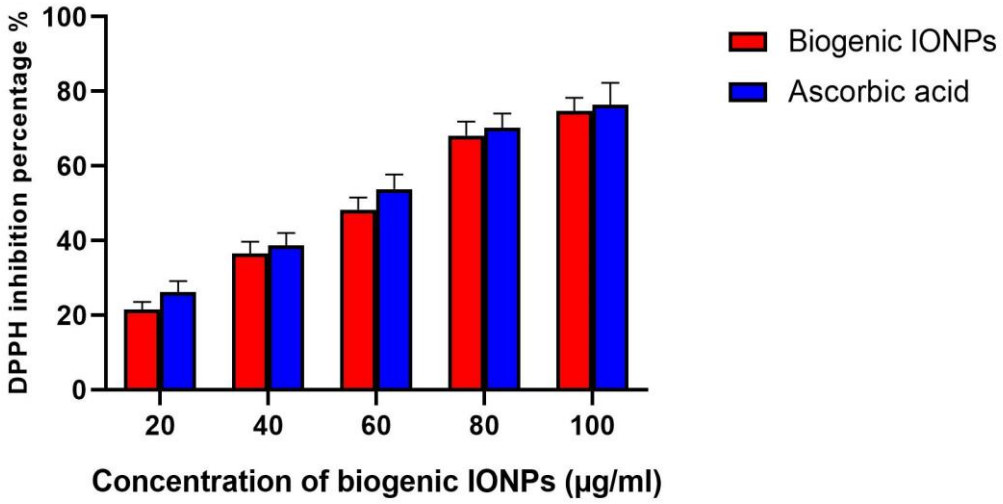

Figure 15. Antiradical efficiency of the biogenic IONPs compared with that of the standard ascorbic acid.

4. Conclusions

The aqueous *Camellia sinensis* leaf extract mediated the green synthesis of amorphous IONPs with an average particle size diameter of 49.63 ± 9.23 nm and a surface charge of –5.69 mV. The biogenic IONPs demonstrated the highest crystal violet dye removal efficiency under sunlight illumination and a 210 min reaction duration. Therefore, the application of biogenic IONPs that are synthesized using leaves from *C. sinensis* for the purpose of removing synthetic dyes such as crystal violet is regarded as a secure, environmentally friendly, and sustainable approach for the remediation of hazardous dyes and the decontamination of the environment, thus promoting a sustainable, eco-friendly, and uncontaminated ecosystem. In addition, the biogenic IONPs exhibited a notable antioxidant activity in comparison with the ascorbic acid standard, suggesting their potential for use in biomedical applications.

Author Contributions: Conceptualization, M.T.Y. and A.A.A.-A.; methodology, M.T.Y.; software, M.T.Y.; validation, M.T.Y. and F.O.A.-O.; formal analysis, M.T.Y., A.A.A.-A. and F.O.A.-O.; investigation, M.T.Y.; resources, A.A.A.-A.; data curation, M.T.Y.; writing—original draft preparation, M.T.Y.; writing—review and editing, M.T.Y., A.A.A.-A. and F.O.A.-O.; visualization, M.T.Y.; supervision, A.A.A.-A. and F.O.A.-O.; project administration, A.A.A.-A.; funding acquisition, M.T.Y. All authors have read and agreed to the published version of the manuscript.

Funding: This research was funded by the Researchers Supporting Project number (RSPD2023R1105), King Saud University, Riyadh, Saudi Arabia.

Data Availability Statement: Not applicable.

Acknowledgments: The authors extend their appreciation to the Researchers Supporting Project number (RSPD2023R1105), King Saud University, Riyadh, Saudi Arabia.

Conflicts of Interest: The authors declare no conflict of interest.

References

1. Saravanan, A.; Senthil Kumar, P.; Jeevanantham, S.; Karishma, S.; Tajsabreen, B.; Yaashikaa, P.R.; Reshma, B. Effective Water/Wastewater Treatment Methodologies for Toxic Pollutants Removal: Processes and Applications towards Sustainable Development. *Chemosphere* **2021**, *280*, 130595. [CrossRef]
2. Chowdhary, P.; Bharagava, R.N.; Mishra, S.; Khan, N. Role of Industries in Water Scarcity and Its Adverse Effects on Environment and Human Health. In *Environmental Concerns and Sustainable Development: Volume 1: Air, Water and Energy Resources*; Shukla, V., Kumar, N., Eds.; Springer: Singapore, 2020; pp. 235–256; ISBN 9789811358890.
3. Gusain, R.; Kumar, N.; Ray, S.S. Recent Advances in Carbon Nanomaterial-Based Adsorbents for Water Purification. *Coord. Chem. Rev.* **2020**, *405*, 213111. [CrossRef]

4. Farhan Hanafi, M.; Sapawe, N. A Review on the Water Problem Associate with Organic Pollutants Derived from Phenol, Methyl Orange, and Remazol Brilliant Blue Dyes. *Mater. Today Proc.* **2020**, *31*, A141–A150. [CrossRef]
5. Li, Y.; Wang, L.; Gao, Y.; Yang, W.; Li, Y.; Guo, C. Porous Metalloporphyrinic Nanospheres Constructed from Metal 5,10,15,20-Tetraksi(4′-Ethynylphenyl)Porphyrin for Efficient Catalytic Degradation of Organic Dyes. *RSC Adv.* **2018**, *8*, 7330–7339. [CrossRef]
6. Karri, R.R.; Ravindran, G.; Dehghani, M.H. Chapter 1-Wastewater—Sources, Toxicity, and Their Consequences to Human Health. In *Soft Computing Techniques in Solid Waste and Wastewater Management*; Karri, R.R., Ravindran, G., Dehghani, M.H., Eds.; Elsevier: Amsterdam, The Netherlands, 2021; pp. 3–33; ISBN 978-0-12-824463-0.
7. Kishor, R.; Purchase, D.; Saratale, G.D.; Saratale, R.G.; Ferreira, L.F.R.; Bilal, M.; Chandra, R.; Bharagava, R.N. Ecotoxicological and Health Concerns of Persistent Coloring Pollutants of Textile Industry Wastewater and Treatment Approaches for Environmental Safety. *J. Environ. Chem. Eng.* **2021**, *9*, 105012. [CrossRef]
8. Vandana; Priyadarshanee, M.; Mahto, U.; Das, S. Chapter 2-Mechanism of Toxicity and Adverse Health Effects of Environmental Pollutants. In *Microbial Biodegradation and Bioremediation*, 2nd ed.; Das, S., Dash, H.R., Eds.; Elsevier: Amsterdam, The Netherlands, 2022; pp. 33–53; ISBN 978-0-323-85455-9.
9. Bhatia, D.; Sharma, N.R.; Singh, J.; Kanwar, R.S. Biological Methods for Textile Dye Removal from Wastewater: A Review. *Crit. Rev. Environ. Sci. Technol.* **2017**, *47*, 1836–1876. [CrossRef]
10. Ahmad, A.; Hamidah Mohd-Setapar, S.; Sing Chuong, C.; Khatoon, A.; Wani, W.A.; Kumar, R.; Rafatullah, M. Recent Advances in New Generation Dye Removal Technologies: Novel Search for Approaches to Reprocess Wastewater. *RSC Adv.* **2015**, *5*, 30801–30818. [CrossRef]
11. Shahadat, M.; Isamil, S. Regeneration Performance of Clay-Based Adsorbents for the Removal of Industrial Dyes: A Review. *RSC Adv.* **2018**, *8*, 24571–24587. [CrossRef]
12. Cai, Z.; Liu, Q.; Li, H.; Wang, J.; Tai, G.; Wang, F.; Han, J.; Zhu, Y.; Wu, G. Waste-to-Resource Strategy to Fabricate Functionalized MOFs Composite Material Based on Durian Shell Biomass Carbon Fiber and Fe_3O_4 for Highly Efficient and Recyclable Dye Adsorption. *Int. J. Mol. Sci.* **2022**, *23*, 5900. [CrossRef]
13. Selim, M.T.; Salem, S.S.; Mohamed, A.A.; El-Gamal, M.S.; Awad, M.F.; Fouda, A. Biological Treatment of Real Textile Effluent Using Aspergillus Flavus and Fusarium Oxysporium and Their Consortium along with the Evaluation of Their Phytotoxicity. *J. Fungi* **2021**, *7*, 193. [CrossRef]
14. Xu, H.; Zhang, Y.; Jiang, Q.; Reddy, N.; Yang, Y. Biodegradable Hollow Zein Nanoparticles for Removal of Reactive Dyes from Wastewater. *J. Environ. Manag.* **2013**, *125*, 33–40. [CrossRef]
15. Khan, F.S.A.; Mubarak, N.M.; Tan, Y.H.; Karri, R.R.; Khalid, M.; Walvekar, R.; Abdullah, E.C.; Mazari, S.A.; Nizamuddin, S. Magnetic Nanoparticles Incorporation into Different Substrates for Dyes and Heavy Metals Removal—A Review. *Environ. Sci. Pollut. Res.* **2020**, *27*, 43526–43541. [CrossRef]
16. Pokrajac, L.; Abbas, A.; Chrzanowski, W.; Dias, G.M.; Eggleton, B.J.; Maguire, S.; Maine, E.; Malloy, T.; Nathwani, J.; Nazar, L.; et al. Nanotechnology for a Sustainable Future: Addressing Global Challenges with the International Network4Sustainable Nanotechnology. *ACS Nano* **2021**, *15*, 18608–18623. [CrossRef] [PubMed]
17. Gatoo, M.A.; Naseem, S.; Arfat, M.Y.; Mahmood Dar, A.; Qasim, K.; Zubair, S. Physicochemical Properties of Nanomaterials: Implication in Associated Toxic Manifestations. *BioMed Res. Int.* **2014**, *2014*, e498420. [CrossRef]
18. Chouke, P.B.; Shrirame, T.; Potbhare, A.K.; Mondal, A.; Chaudhary, A.R.; Mondal, S.; Thakare, S.R.; Nepovimova, E.; Valis, M.; Kuca, K. Bioinspired Metal/Metal Oxide Nanoparticles: A Road Map to Potential Applications. *Mater. Today Adv.* **2022**, *16*, 100314. [CrossRef]
19. Saied, E.; Salem, S.S.; Al-Askar, A.A.; Elkady, F.M.; Arishi, A.A.; Hashem, A.H. Mycosynthesis of Hematite (α-Fe_2O_3) Nanoparticles Using Aspergillus Niger and Their Antimicrobial and Photocatalytic Activities. *Bioengineering* **2022**, *9*, 397. [CrossRef]
20. Shafey, A.M.E. Green Synthesis of Metal and Metal Oxide Nanoparticles from Plant Leaf Extracts and Their Applications: A Review. *Green Process. Synth.* **2020**, *9*, 304–339. [CrossRef]
21. Nagajyothi, P.C.; Prabhakar Vattikuti, S.V.; Devarayapalli, K.C.; Yoo, K.; Shim, J.; Sreekanth, T.V.M. Green Synthesis: Photocatalytic Degradation of Textile Dyes Using Metal and Metal Oxide Nanoparticles-Latest Trends and Advancements. *Crit. Rev. Environ. Sci. Technol.* **2020**, *50*, 2617–2723. [CrossRef]
22. Jadoun, S.; Arif, R.; Jangid, N.K.; Meena, R.K. Green Synthesis of Nanoparticles Using Plant Extracts: A Review. *Environ. Chem. Lett.* **2021**, *19*, 355–374. [CrossRef]
23. Nagra, U.; Shabbir, M.; Zaman, M.; Mahmood, A.; Barkat, K. Review on Methodologies Used in the Synthesis of Metal Nanoparticles: Significance of Phytosynthesis Using Plant Extract as an Emerging Tool. *Curr. Pharm. Des.* **2020**, *26*, 5188–5204. [CrossRef]
24. Baruah, S.; Dutta, J. Nanotechnology Applications in Pollution Sensing and Degradation in Agriculture: A Review. *Environ. Chem. Lett.* **2009**, *7*, 191–204. [CrossRef]
25. Zhang, H.; Tian, W.; Wang, S. Photocatalytic Oxygen Evolution. In *Solar-to-Chemical Conversion*; John Wiley & Sons, Ltd.: Hoboken, NJ, USA, 2021; pp. 129–162; ISBN 978-3-527-82507-3.
26. Nande, A.; Raut, S.; Michalska-Domanska, M.; Dhoble, S.J. Green Synthesis of Nanomaterials Using Plant Extract: A Review. *Curr. Pharm. Biotechnol.* **2021**, *22*, 1794–1811. [CrossRef] [PubMed]
27. Vinu, R.; Madras, G. Renewable Energy via Photocatalysis. *Curr. Org. Chem.* **2013**, *17*, 2538–2558. [CrossRef]

28. Cai, M.; Liu, Y.; Wang, C.; Lin, W.; Li, S. Novel $Cd_{0.5}Zn_{0.5}S/Bi_2MoO_6$ S-Scheme Heterojunction for Boosting the Photodegradation of Antibiotic Enrofloxacin: Degradation Pathway, Mechanism and Toxicity Assessment. *Sep. Purif. Technol.* **2023**, *304*, 122401. [CrossRef]
29. Su, R. Photocatalysis for Pollution Remediation. In *UV-Visible Photocatalysis for Clean Energy Production and Pollution Remediation*; John Wiley & Sons, Ltd.: Hoboken, NJ, USA, 2023; pp. 267–283; ISBN 978-3-527-83799-1.
30. Etacheri, V.; Di Valentin, C.; Schneider, J.; Bahnemann, D.; Pillai, S.C. Visible-Light Activation of TiO_2 Photocatalysts: Advances in Theory and Experiments. *J. Photochem. Photobiol. C Photochem. Rev.* **2015**, *25*, 1–29. [CrossRef]
31. Wu, Z.; Yang, J.; Shao, W.; Cheng, M.; Luo, X.; Zhou, M.; Li, S.; Ma, T.; Cheng, C.; Zhao, C. High-Valence Transition Metal Modified FeNiV Oxides Anchored on Carbon Fiber Cloth for Efficient Oxygen Evolution Catalysis. *Adv. Fiber Mater.* **2022**, *4*, 774–785. [CrossRef]
32. Li, S.; Cai, M.; Wang, C.; Liu, Y. Ta_3N_5/CdS Core–Shell S-Scheme Heterojunction Nanofibers for Efficient Photocatalytic Removal of Antibiotic Tetracycline and Cr(VI): Performance and Mechanism Insights. *Adv. Fiber Mater.* **2023**, *5*, 994–1007. [CrossRef]
33. Li, X.; Liu, T.; Zhang, Y.; Cai, J.; He, M.; Li, M.; Chen, Z.; Zhang, L. Growth of BiOBr/ZIF-67 Nanocomposites on Carbon Fiber Cloth as Filter-Membrane-Shaped Photocatalyst for Degrading Pollutants in Flowing Wastewater. *Adv. Fiber Mater.* **2022**, *4*, 1620–1631. [CrossRef]
34. Li, S.; Yan, R.; Cai, M.; Jiang, W.; Zhang, M.; Li, X. Enhanced Antibiotic Degradation Performance of $Cd_{0.5}Zn_{0.5}S/Bi_2MoO_6$ S-Scheme Photocatalyst by Carbon Dot Modification. *J. Mater. Sci. Technol.* **2023**, *164*, 59–67. [CrossRef]
35. Li, H.; Zhao, H.; Li, C.; Li, B.; Tao, B.; Gu, S.; Wang, G.; Chang, H. Redox Regulation of Photocatalytic Nitrogen Reduction Reaction by Gadolinium Doping in Two-Dimensional Bismuth Molybdate Nanosheets. *Appl. Surf. Sci.* **2022**, *600*, 154105. [CrossRef]
36. Bharathi, D.; Preethi, S.; Abarna, K.; Nithyasri, M.; Kishore, P.; Deepika, K. Bio-Inspired Synthesis of Flower Shaped Iron Oxide Nanoparticles (FeONPs) Using Phytochemicals of Solanum Lycopersicum Leaf Extract for Biomedical Applications. *Biocatal. Agric. Biotechnol.* **2020**, *27*, 101698. [CrossRef]
37. Yassin, M.T.; Elgorban, A.M.; Al-Askar, A.A.; Sholkamy, E.N.; Ameen, F.; Maniah, K. Synergistic Anticandidal Activities of Greenly Synthesized ZnO Nanomaterials with Commercial Antifungal Agents against Candidal Infections. *Micromachines* **2023**, *14*, 209. [CrossRef]
38. Mirza, A.U.; Kareem, A.; Nami, S.A.A.; Khan, M.S.; Rehman, S.; Bhat, S.A.; Mohammad, A.; Nishat, N. Biogenic Synthesis of Iron Oxide Nanoparticles Using Agrewia Optiva and Prunus Persica Phyto Species: Characterization, Antibacterial and Antioxidant Activity. *J. Photochem. Photobiol. B* **2018**, *185*, 262–274. [CrossRef] [PubMed]
39. Liu, X.; Dai, D.; Cui, Z.; Zhang, Q.; Gong, X.; Wang, Z.; Liu, Y.; Zheng, Z.; Cheng, H.; Dai, Y.; et al. Optimizing the Reaction Pathway by Active Site Regulation in the CdS/Fe_2O_3 Z-Scheme Heterojunction System for Highly Selective Photocatalytic Benzylamine Oxidation Integrated with H2 Production. *ACS Catal.* **2022**, *12*, 12386–12397. [CrossRef]
40. Rajendran, A.; Alsawalha, M.; Alomayri, T. Biogenic Synthesis of Husked Rice-Shaped Iron Oxide Nanoparticles Using Coconut Pulp (*Cocos Nucifera* L.) Extract for Photocatalytic Degradation of Rhodamine B Dye and Their in Vitro Antibacterial and Anticancer Activity. *J. Saudi Chem. Soc.* **2021**, *25*, 101307. [CrossRef]
41. Batool, T.; Shah, Z.H.; Ashraf, H.; Ali, D.; Shamaila, S.; Anjum, T.; Naseem, S.; Riaz, S. Solar Energy Driven Photo Catalytic Action and Antimicrobial Activities of Iron Oxide Nanoparticles. *J. Sol-Gel Sci. Technol.* **2023**, 1–17. [CrossRef]
42. Pang, Y.L.; Lim, S.; Ong, H.C.; Chong, W.T. Research Progress on Iron Oxide-Based Magnetic Materials: Synthesis Techniques and Photocatalytic Applications. *Ceram. Int.* **2016**, *42*, 9–34. [CrossRef]
43. Al-Tamimi, S.A. Biogenic Green Synthesis of Metal Oxide Nanoparticles Using Oat Biomass for Ultrasensitive Modified Polymeric Sensors. *Green Chem. Lett. Rev.* **2021**, *14*, 166–179. [CrossRef]
44. Dejen, K.D.; Zereffa, E.A.; Murthy, H.C.A.; Merga, A. Synthesis of ZnO and ZnO/PVA Nanocomposite Using Aqueous Moringa Oleifeira Leaf Extract Template: Antibacterial and Electrochemical Activities. *Rev. Adv. Mater. Sci.* **2020**, *59*, 464–476. [CrossRef]
45. Omran, B.A.; Aboelazayem, O.; Nassar, H.N.; El-Salamony, R.A.; El-Gendy, N.S. Biovalorization of Mandarin Waste Peels into Silver Nanoparticles and Activated Carbon. *Int. J. Environ. Sci. Technol.* **2021**, *18*, 1119–1134. [CrossRef]
46. Ranjani, S.; Priya, P.S.; Veerasami, M.; Hemalatha, S. Novel Polyherbal Nanocolloids to Control Bovine Mastitis. *Appl. Biochem. Biotechnol.* **2022**, *194*, 246–265. [CrossRef] [PubMed]
47. Yadav, V.K.; Yadav, K.K.; Gnanamoorthy, G.; Choudhary, N.; Khan, S.H.; Gupta, N.; Kamyab, H.; Bach, Q.-V. A Novel Synthesis and Characterization of Polyhedral Shaped Amorphous Iron Oxide Nanoparticles from Incense Sticks Ash Waste. *Environ. Technol. Innov.* **2020**, *20*, 101089. [CrossRef]
48. Yadav, V.K.; Gnanamoorthy, G.; Ali, D.; Bera, S.P.; Roy, A.; Kumar, G.; Choudhary, N.; Kalasariya, H.; Basnet, A. Cytotoxicity, Removal of Congo Red Dye in Aqueous Solution Using Synthesized Amorphous Iron Oxide Nanoparticles from Incense Sticks Ash Waste. *J. Nanomater.* **2022**, *2022*, e5949595. [CrossRef]
49. Yadav, V.K.; Ali, D.; Khan, S.H.; Gnanamoorthy, G.; Choudhary, N.; Yadav, K.K.; Thai, V.N.; Hussain, S.A.; Manhrdas, S. Synthesis and Characterization of Amorphous Iron Oxide Nanoparticles by the Sonochemical Method and Their Application for the Remediation of Heavy Metals from Wastewater. *Nanomaterials* **2020**, *10*, 1551. [CrossRef]
50. Hasany, S.F.; Abdurahman, N.H.; Sunarti, A.R.; Jose, R. Magnetic Iron Oxide Nanoparticles: Chemical Synthesis and Applications Review. *Curr. Nanosci.* **2013**, *9*, 561–575. [CrossRef]
51. Yan, S.; Abhilash, K.P.; Tang, L.; Yang, M.; Ma, Y.; Xia, Q.; Guo, Q.; Xia, H. Research Advances of Amorphous Metal Oxides in Electrochemical Energy Storage and Conversion. *Small* **2019**, *15*, 1804371. [CrossRef] [PubMed]

52. Chavali, M.S.; Nikolova, M.P. Metal Oxide Nanoparticles and Their Applications in Nanotechnology. *SN Appl. Sci.* **2019**, *1*, 607. [CrossRef]
53. Natarajan, S.; Harini, K.; Gajula, G.P.; Sarmento, B.; Neves-Petersen, M.T.; Thiagarajan, V. Multifunctional Magnetic Iron Oxide Nanoparticles: Diverse Synthetic Approaches, Surface Modifications, Cytotoxicity towards Biomedical and Industrial Applications. *BMC Mater.* **2019**, *1*, 2. [CrossRef]
54. Dash, A.; Ahmed, M.T.; Selvaraj, R. Mesoporous Magnetite Nanoparticles Synthesis Using the Peltophorum Pterocarpum Pod Extract, Their Antibacterial Efficacy against Pathogens and Ability to Remove a Pollutant Dye. *J. Mol. Struct.* **2019**, *1178*, 268–273. [CrossRef]
55. Ekwumemgbo, P.A.; Shallangwa, G.A.; Okon, I.E. Green Synthesis and Characterization of Iron Oxide Nanoparticles Using Prosopis Africana Leaf Extract. *Commun. Phys. Sci.* **2023**, *9*, 125–136.
56. Mishra, A.K.; Ramaprabhu, S. Nano Magnetite Decorated Multiwalled Carbon Nanotubes: A Robust Nanomaterial for Enhanced Carbon Dioxide Adsorption. *Energy Environ. Sci.* **2011**, *4*, 889–895. [CrossRef]
57. Vinayagam, R.; Pai, S.; Varadavenkatesan, T.; Narasimhan, M.K.; Narayanasamy, S.; Selvaraj, R. Structural Characterization of Green Synthesized α-Fe_2O_3 Nanoparticles Using the Leaf Extract of Spondias Dulcis. *Surf. Interfaces* **2020**, *20*, 100618. [CrossRef]
58. Alqarni, L.S.; Alghamdi, M.D.; Alshahrani, A.A.; Nassar, A.M. Green Nanotechnology: Recent Research on Bioresource-Based Nanoparticle Synthesis and Applications. *J. Chem.* **2022**, *2022*, e4030999. [CrossRef]
59. Martins, E.S.; Espindola, A.; Britos, T.N.; Chagas, C.; Barbosa, E.; Castro, C.E.; Fonseca, F.L.A.; Haddad, P.S. Potential Use of DMSA-Containing Iron Oxide Nanoparticles as Magnetic Vehicles against the COVID-19 Disease. *ChemistrySelect* **2021**, *6*, 7931–7935. [CrossRef]
60. Bhatnagar, S.; Kobori, T.; Ganesh, D.; Ogawa, K.; Aoyagi, H. Biosynthesis of Silver Nanoparticles Mediated by Extracellular Pigment from Talaromyces Purpurogenus and Their Biomedical Applications. *Nanomaterials* **2019**, *9*, 1042. [CrossRef] [PubMed]
61. Baldi, F.; Marchetto, D.; Paganelli, S.; Piccolo, O. Bio-Generated Metal Binding Polysaccharides as Catalysts for Synthetic Applications and Organic Pollutant Transformations. *New Biotechnol.* **2011**, *29*, 74–78. [CrossRef] [PubMed]
62. Aljeldah, M.M.; Yassin, M.T.; Mostafa, A.A.-F.; Aboul-Soud, M.A. Synergistic Antibacterial Potential of Greenly Synthesized Silver Nanoparticles with Fosfomycin Against Some Nosocomial Bacterial Pathogens. *Infect. Drug Resist.* **2023**, *16*, 125–142. [CrossRef]
63. Khan, A.; Roy, A.; Bhasin, S.; Emran, T.B.; Khusro, A.; Eftekhari, A.; Moradi, O.; Rokni, H.; Karimi, F. Nanomaterials: An Alternative Source for Biodegradation of Toxic Dyes. *Food Chem. Toxicol.* **2022**, *164*, 112996. [CrossRef]
64. Zhang, W.; Tang, J.; Ye, J. Structural, Photocatalytic, and Photophysical Properties of Perovskite $MSnO_3$ (M = Ca, Sr, and Ba) Photocatalysts. *J. Mater. Res.* **2007**, *22*, 1859–1871. [CrossRef]
65. Bryukhanov, V.V.; Minaev, B.M.; Tsibul'nikova, A.V.; Slezhkin, V.A. The Effect of Gold Nanoparticles on Exchange Processes in Collision Complexes of Triplet and Singlet Oxygen Molecules with Excited Eosin Molecules. *Opt. Spectrosc.* **2015**, *119*, 29–38. [CrossRef]
66. Mishra, M.; Chun, D.-M. α-Fe_2O_3 as a Photocatalytic Material: A Review. *Appl. Catal. Gen.* **2015**, *498*, 126–141. [CrossRef]
67. Muthukumar, H.; Chandrasekaran, N.I.; Mohammed, S.N.; Pichiah, S.; Manickam, M. Iron Oxide Nano-Material: Physicochemical Traits and in Vitro Antibacterial Propensity against Multidrug Resistant Bacteria. *J. Ind. Eng. Chem.* **2017**, *45*, 121–130. [CrossRef]
68. Bishnoi, S.; Kumar, A.; Selvaraj, R. Facile Synthesis of Magnetic Iron Oxide Nanoparticles Using Inedible Cynometra Ramiflora Fruit Extract Waste and Their Photocatalytic Degradation of Methylene Blue Dye. *Mater. Res. Bull.* **2018**, *97*, 121–127. [CrossRef]
69. Mansour, A.T.; Alprol, A.E.; Abualnaja, K.M.; El-Beltagi, H.S.; Ramadan, K.M.A.; Ashour, M. The Using of Nanoparticles of Microalgae in Remediation of Toxic Dye from Industrial Wastewater: Kinetic and Isotherm Studies. *Materials* **2022**, *15*, 3922. [CrossRef] [PubMed]
70. Mahmoud, M.E.; El-Sharkawy, R.M.; Ibrahim, G.A.A. A Novel Bionanocomposite from Doped Lipase Enzyme into Magnetic Graphene Oxide-Immobilized-Cellulose for Efficient Removal of Methylene Blue and Malachite Green Dyes. *J. Mol. Liq.* **2022**, *368*, 120676. [CrossRef]